DESIGN AND FABRICATION OF NANOSTRUCTURES FOR THERMAL CONDUCTIVITY MEASUREMENTS AND PICOSECOND ACOUSTICS

BY

JUNG-HYUN LEE

THESIS

Submitted in partial fulfillment of the requirements
for the degree of Master of Science in Mechanical Engineering
in the Graduate College of the
University of Illinois at Urbana-Champaign, 2010

Urbana, Illinois

Adviser:

Assistant Professor Sanjiv Sinha

ABSTRACT

This thesis describes three fabrication processes for measurement in three different phonon applications. First, fabrication of sub-10nm fluorocarbon films is presented for thin film thermal conductivity measurement. Thermal conductivity of this ultra-thin polymer film is especially interested in phonon study due to its atomic confinement in one dimension. Using plasma polymerization technique, sub-10 nm polymer film can be easily deposited by reactive ion etching system (RIE) with 80 sccm of CHF_3 flow rate, 80W of RF power, and 150 mTorr of pressure. Bonding components of these polymers are also analyzed by x-ray photo-electron spectroscopy (XPS). Second, fabrication of MEMS platform for thermal conductivity measurement in single nanowire is presented. Thermal conductivity of single nanowire is interested especially for Si nanowire with rough surface for efficient thermoelectric device. This MEMS platform is design to have capability of measuring not only thermal conductivity but also Seebeck coefficient and electrical conductivity. E-beam lithography and optical lithography with oxygen plasma etching are used to pattern sub-micron patterning and TMAH wet etching and XeF_2 etching are used to release the structures to free standing. Last, fabrication of metallic gratings is presented for picosecond acoustics. Generating and detecting picosecond acoustics are interested especially for terahertz regime. We have fabricated aluminum gratings with 300nm and 400nm period with different duty cycle (η=w/p, where w is width of gratings and p is period of gratings). We have verified that generating surface acoustic frequency was determined by its period and higher duty cycle leads higher attenuation of the signal.

ACKNOWLEDGMENTS

First, I deeply thank my Lord for always leading me into righteous way and being with me. I would like to thank Prof. Sanjiv Sinha for guiding and supporting my research with mentorship and encouragement throughout my studies at University of Illinois at Urbana-Champaign.

I would like to acknowledge my co-workers. I thank Marc Ghossoub for thermal conductivity measurement for plasma polymerized polymer films. I show gratitude to Oksen Baris for thickness analysis and surface analysis of the polymer films. I express thanks to Jyothi Sadhu for helping me to understand theoretical background of thermoelastic model of picosecond acoustics. I am also grateful to staffs in Micro Nano Technology Laboratory and Materials Research Laboratory for providing valuable advices on my research. It was great pleasure to discuss about overall research with each staffs.

Finally, I would like to acknowledge my family. I especially show gratitude to my beloved wife, Yunhee Im, for her support and many sacrifices. I also thank my parents for their support and great advices. Lastly, I am also grateful for the prayer of Pastor Choi and Yoon and the congregation at my church.

TABLE OF CONTENTS

List of Tables vi

List of Figures vii

CHAPTER 1 INTRODUCTION 1

1.1 OBJECTIVE 1

1.2 OVERVIEW. 2

CHAPTER 2 LITERATURE REVIEW 4

2.1 FABRICATION OF FLUOROCARBON FILMS 4

2.2 MEASUREMENT PLATFORMS FOR THERMAL CONDUCTIVITY OF NANOWIRES/TUBES 6

2.3 PICOSECOND ACOUSTICS IN METALLIC GRATINGS 7

CHAPTER 3 PLASMA POLYMERIZATION OF SUB-10NM FLUOROCARBON FILMS 10

3.1 PLASMA POLYMERIZATION PROCESS 10

3.2 SURFACE AND BULK CHARACTERIZATION 11

CHAPTER 4 DESIGN AND FABRICATION OF THERMAL CONDUCTIVITY MEASUREMENT PLATFORM 15

4.1 DESIGN OVERVIEW 15

4.2 THERMAL CONDUCTANCE ANALYSIS 17

4.3 FILM STRESS ANALYSIS 21

4.4 FABRICATION USING E-BEAM LITHOGRAPHY AND TMAH ETCHING 22

4.5 PROBLEMS AND TRIAL SOLUTIONS 24

4.6 FABRICATION USING OPTICAL LITHOGRAPHY AND XeF_2 ETCHING 26

CHAPTER 5 METALLIC GRATINGS FOR GENERATING GHz SURFACE PHONONS 30

5.1 FABRICATION OF ALUMINUM GRATINGS 30

5.2 GENERATING GHz SURFACE PHONONS 31

CHAPTER 6 SUMMARY 36

REFERENCES 37

APPENDIX A. MASK DESIGN 39

APPENDIX B. ANSYS ANALYSIS CODE 42

List of Tables

TABLE 3.1. Functional groups and corresponding binding energies as identified from a Gaussian-Lorentzian curve fitting of the C1s core level XPS spectra 13

TABLE 4.1. Summary of film stress analysis 21

List of Figures

FIGURE 2.1. Picosecond ultrasonic laser system 9

FIGURE 3.1. C1s core-level XPS spectra of the fluorocarbon films showing a change in film composition at different film thickness 14

FIGURE 4.1. Schematic of device design 16

FIGURE 4.2 Fabrication process flow for creating gap with various lengths: (a) membrane is connected by a bridge. (b) bridge is disconnected by FIB. (c) Si nanowire is placed in between two membrane 16

FIGURE 4.3. Schematic of simple thermal circuit diagram of the device 17

FIGURE 4.4. Plot of thermal conductivity of supporting beam comparing with design of Li Shi et al. 18

FIGURE 4.5. ANSYS 2D temperature distribution analysis of (a) heating membrane and (b) sensing membrane at 300K 20

FIGURE 4.6. SEM images of structures before releasing step 23

FIGURE 4.7. Free standing membranes and defects in contact pads 24

FIGURE 4.8. Example of stiction problems 25

FIGURE 4.9. O_2 plasma etching of AZ 5214 patterns: (a), (b) before etching (c), (d) after 10 minutes etching 26

FIGURE 4.10. 300nm Pt heater lines done by optical lithography 28

FIGURE 4.11. Free standing structure done by XeF_2 etching 28

FIGURE 4.12. Broken free standing structures due to the film stress 29

FIGURE 5.1. SEM images of aluminum gratings 30

FIGURE 5.2. Diagram of pump-and-probe system 31

FIGURE 5.3. (a) Relative change of reflectivity in function of delay time for grating with 424 nm period and 290 nm grating width. (b) Relative change of reflectivity which thermal background is removed by filter 33

FIGURE 5.4. Power of Fourier transform in frequency domain for (a) 320 nm

grating period and (b) 424 nm grating period with different aluminum width 34

FIGURE 5.5. Power of the highest peak from Fourier transform in function of ratio of grating width to grating period 35

FIGURE A.1. Overlapping all mask designs of one device 39

FIGURE A.2. Mask design of interconnection between heater lines and contact pads 39

FIGURE A.3. Mask design of contact pads 40

FIGURE A.4. Example of the spacers 40

FIGURE A.5. Mask design of modified heater lines with 1μm width 41

CHAPTER 1

INTRODUCTION

1.1 OBJECTIVE

A lattice of atoms in a uniform solid material undergoes vibrations at any finite temperature. These vibrations are in the form of collective modes that extend over the entire solid. The collective vibrational modes can possess only discrete amounts of energy, and this quantized energy is called a phonon. The study of phonons is important for research into physical properties of solid, such as thermal conductivity, electrical conductivity, and so on. Phonons in confined structures are interesting for engineering applications, especially centered around thermal sciences such as ultra-thin films, nanowires, nanotubes, and quantum dots.

This thesis describes three fabrication processes of nanostructures for thermal conductivity measurements and picosecond acoustics with the intention of studying phonon transport. First, we describes the plasma polymerization of a fluorocarbon film that is fabricated within sub-10nm thickness. This fabrication technique is useful for applications in the nanoelectronics industry due to the uniformity of the film and the convenient process of fabrication. In another related work, we have measured and modeled the thermal conductivity of these ultra-thin films.[38] Second, we have fabricated a MEMS platform for thermal conductivity measurements of nanostructures. This device has the capability of measuring the thermal conductivities of one-dimensional nanostructures such as nanowires and nanotubes. The platform will be used to measure thermal conductivity of single Si nanowires with rough surfaces which are interesting for thermoelectric applications. The rough surface lowers the thermal conductivity

due to phonon back-scattering and leads to higher efficiency of thermoelectric energy conversion. Finally, we have fabricated aluminum gratings for generating GHz surface phonons. In another related work,[39] we have described the use of these gratings for studying mass loading at approximately 15 GHz frequencies in silicon.

1.2 OVERVIEW

Chapter 3 presents details of the fabrication of plasma polymerized fluorocarbon films for ultrafast measurements of thermal transport. Plasma polymerization is the polymer deposition technique using plasma to ionize gas molecules and initiate formation of polymer on the substrate surface. We characterize the thin films by X-ray photoelectron spectroscopy (XPS), atomic force microscopy (AFM), and spectroscopic ellipsometry and measure polymer thicknesses ranging from 37 nm down to 2 nm. XPS data shows that the fluorine to carbon ratio is 0.65 for a 2 nm film and increases to 1.3 for the thickest film, 37 nm.

Chapter 4 presents design and fabrication of a MEMS platform which can measure the thermal conductivity of individual silicon nanowires in the expected thermal conductivity as low as 1 W/mK. This device has two suspended membranes that are laterally supported by six beams each. Metallic heater lines are embedded on each membrane for not only raising temperature of the membrane but also for measuring the temperature of the membrane. Thermal conductance analysis and film stress analysis verify thermal isolation and mechanical stability of the structures. For patterning sub-micron metallic heater lines, two methods have been tried: E-beam lithography and optical lithography with O_2 plasma etching technique. For releasing structures to free standing structures, TMAH etching and XeF_2 etching has been used.

Chapter 5 presents fabrication of aluminum gratings for picosecond acoustics. Aluminum gratings are fabricated by combination of e-beam lithography and liftoff technique. These metallic gratings have period of around 300 nm and 400 nm with different widths. We use ultrafast laser pulses absorbed in these metallic gratings to generate surface acoustic waves in an underlying silicon substrate. Our measurements show that the frequency of the surface wave depends on the periodicity of the grating but is independent of the width of the individual metallic lines. However, the power decays non-linearly as the duty cycle of the grating increases.

CHAPTER 2

LITERATURE REVIEW

2.1 FABRICATION OF FLUOROCARBON FILMS

Polymers are industrially interesting materials that may contribute inexpensive solutions to nanoscale heat transfer and its numerous applications.[1] In fact, polymers exhibit a shift in their thermal properties when confined to nanometer scales. For instance, ultrathin polymers, with thicknesses comparable to the radius of gyration, show a glass transition temperature that is both different from the bulk and largely dependent on surface interactions.[2] Furthermore, incoherent neutron scattering studies[3] on confined ultrathin films reveal a suppression of anharmonicity near the glass transition but its impact on thermal transport is not well understood at present.

While bulk thermal properties have been extensively studied for a variety of polymers, published thermal conductivity measurements for thin polymer films typically cover thicknesses greater than 100 nm. Kurabayashi et al. showed that the thermal conductivity of polyimide films is anisotropic and independent of thickness for polymers exceeding 500 nm.[4] A more recent study on polyaniline[5] measured a five-fold decrease in thermal conductivity when the film thickness is decreased from 5 μm to 110 nm.

The fabrication techniques to create ultra-thin polymer films have been reported in many studies. Torkelson et al. reports fabrication of spin coated ultra-thin polystyrene films and poly (methyl methacrylate) (PMMA) films with thickness ranging from 10nm to 33um.[33] Also, they proposed simple model to predict thickness of the film as a function of process parameters, such as initial properties of the polymer solution, solvent, and spin speed. This model predicts the film

thickness within 10 % in thickness range from 10 nm to 33 um. The advantage of spin coting technique is convenient and inexpensive in fabrication. However, the disadvantage is difficulty of controlling thickness in sub-10nm scale, because thickness can be easily changed by small alteration of spin speed and solvent concentration. Koumoto et al. reports fabrication of self-assembled monolayers (SAMs) on flexible substrate.[34] They have successfully fabricated the SAMs of octadecyltrichlorosilane (OTS), phenyltrichlorosilane (PTCS), vinyltrichlorosilane (VTCS), and *p*-tolyltrichlorosilane (TTCS) on poly (ethylene terephthalate) (PET) surface. The properties of SAMs were controlled by adjusting immersing time of the substrates in the solution and the concentration of the solution. The advantage of this fabrication technique is capability of sub-5nm depending on the kind of polymers. However, the disadvantage is the thickness is limited by length of the single polymer chain and limited material can be deposited.

Plasma polymerization is another widely used polymer deposition technique. Bougdira et al. reports the fabrication of CHF_3 plasma-polymerized fluorocarbon films with thickness ranging from 0.3 μm to 1.5 μm.[35] These low dielectric fluorocarbon films are being studied for various applications such as substitutive material for conventional SiO_2 in integral circuit to reduce power consumption, passivation layer for Bosch process in deep reactive ion etching (DRIE), and so on[6]. Also, they are useful material for biocompatible and low friction coating due to their hydrophobicity and smooth low energy surface.[7,8] We have extensively studied this CHF_3 plasma polymerized films and successfully fabricated ultra-thin polymer film up to 2nm thickness.

2.2 MEASUREMENT PLATFORMS FOR THERMAL CONDUCTIVITY OF NANOWIRES/TUBES

Thermoelectric device enables to convert thermal energy to electrical energy. However commercial thermoelectric device operates at about 10% of Carnot efficiency, while a kitchen refrigerator operates at about 30 % of Carnot efficiency.[9] The efficiency of thermoelectric device is often represented by figure of merit, ZT. ZT can be defined as $(S\sigma/\kappa) \times T$, where S is Seebeck coefficient, σ is electrical conductivity, and κ is thermal conductivity. The thermoelectric materials or devices are being studying to increase Seebeck coefficient and electrical conductivity and to decrease thermal conductivity, because higher value of ZT gives higher device efficiency. However, most bulk materials have increasing thermal conductivity when its electrical conductivity tends to increase. This problem has been limited having higher ZT and, for the solution of this problem, many researchers have been studying on nanostructures such as nanowire, nanotubes, and so on.[10,11]

The measurements of low dimensional nanostructures require fabricating MEMS device with high thermal isolation. For instance, Li Shi et al. have reported scanning thermal microscopy on carbon nanotubes using batch fabricated AFM tips.[36] This device has capability of imaging temperature distribution of electrically heated carbon nanotubes with around 50 nm of spatial resolution. Within this resolution, the device offers promising prospect of thermal transport of a low dimensional nanostructure. In the other hand, Boukai et al. designed and fabricated device for array of Si nanowires, especially for Si nanowires with rough surface.[10] They used SOI wafers to fabricated array of nanowires on suspended structure. However, this MEMS platform can only measure patterned Si nanowires and cannot substitute Si nanowire to other nanostructures such as carbon nanotubes. Similarly, Li Shi et al. fabricated a device that

can measure any single nanowire or nanotube.[11] Their devices are also suspended structure to thermally isolate device from environments. The device contains two separate suspended membranes, which are supported by 5 beams each. Each membrane contains metal heater coils for increasing temperature and also for measuring temperature. For the measurement, nanowire sits between these two membranes. One of the membranes is heated by applying current through the metal heater coil. Thus, temperature gradient is generated across the nanowire, and temperature can be measured by four probe measurement. However, their design restricts the length of the nanowire by fixed gap between two membranes, approximately 4 μm. We have extensively studied this design in order to measure thermal conductivities of shorter length of single nanowire or nanotube.

2.3 PICOSECOND ACOUSTICS IN METALLIC GRATINGS

Surface acoustic waves (SAW) are important especially in signal processing in electrical system[12]. Its low velocity comparing to light velocity and shorter wavelength enable to make compact device. Current technologies of generating SAW are limited to gigahertz (GHz) range. Many research groups have been investigated to generate SAW in frequency of terahertz (THz) range. Generating SAW in near THz regime enables to develop ultrafast wireless communication device and biosensing device.[13] There are also many possible signal processing applications such as delay lines, bandpass filters, ultrahigh oscillator control elements, programmable devices for frequency and time domain filtering, frequency synthesizers and correlator.[14,15]

There are several different methods to generate and detect SAW. Most widely used and fundamental component for SAW generation is inter-digital transducers (IDT). IDT uses piezoelectric film with lithographically patterned thin metallic film as countered electrodes, and

electric field occurred by those electrodes leads periodic strains on piezoelectric film which generates SAW.[16,17] In similar principle but simpler design in fabrication-wise, we uses picoseconds ultrasonic laser system to generate SAW. Picosecond ultrasonic method has been widely used to generate and detect acoustic signals in thin films and nanostructures due to its noncontact measurability.[18] Figure 2.1 shows basic schematic of picosecond ultrasonic technology using aluminum periodic grating structures. This technique generates SAW applying laser pulse onto grating structures which is fabricated with laser absorbing material such as aluminum. When laser pulse hits such grating structures, thermal expansion occurs each grating due to its energy absorption of aluminum grating from the laser pulse. Since each grating is periodically spaced, spatially varying thermal expansion occurs and such instantaneous expansions generate SAW. Previous work by Antonelli et al. was able to generate sub 10 GHz SAW using around 1 μm grating structure.[19] Hurley et al. was able to generate 22.4 GHz SAW with 220 nm aluminum grating period fabricated by e-beam lithography.[20] Recently, Siemens et al. has successfully generated nearly 50 GHz SAW using nickel-on-sapphire nanostructures and wavelength as short as 125 nm.[21] Improving picoseconds ultrasonic technique to high GHz or near THz regime requires more studies on material and laser properties which affect on frequency and intensity of SAW and controlling those parameters to enhance its signal. In this thesis, our study focuses on effect of grating width on frequency and strength of SAW signal.

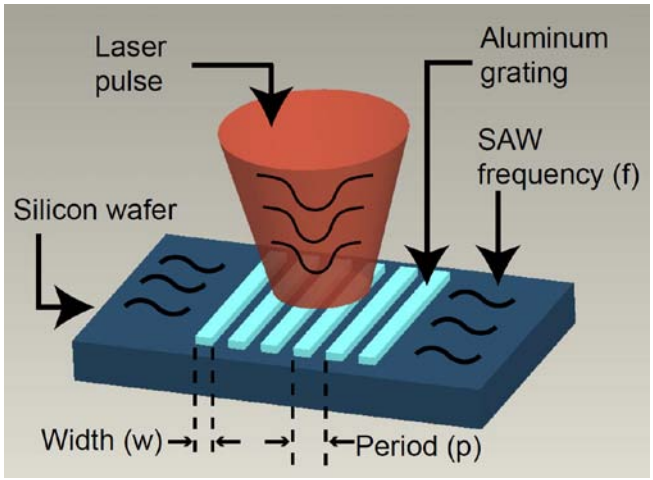


FIGURE 2.1. Picosecond ultrasonic laser system.

CHAPTER 3

PLASMA POLYMERIZATION OF SUB-10NM FLUOROCARBON FILMS

3.1 PLASMA POLYMERIZATION PROCESS

We deposited the amorphous fluorocarbon films (a-C:F) on a polished, RCA cleaned silicon wafer using plasma polymerization from a CHF3 monomer gas flowing at 80 sccm with a base pressure of 150 mTorr and an RF power of 80W. The deposition rate was approximately 1.4 Å/sec and thickness independent. The rate of plasma polymerization on the surface of a wafer in a reactive ion etcher (RIE) depends on the chemistry of the gases forming the plasma, the gas flow rates, the RF power driving the plasma, the electrodes bias and the local chemistry at the surface of the wafer. In particular, the same is true for plasma polymerization of fluorocarbons.[22] At low RF powers, the rate of polymer deposition from a fluorocarbon monomer gas exceeds the etching rate and can be controlled to within a few angstroms per second. The RF ionized CFx gas radicals react with the Si surface and the surrounding gas phase to form a highly cross-linked network of C-Fx (x = 1-3) bonds, C-C bonds and C-CFx cross-links. The film's cross-linking density increases with RF power, which allows for accurate tailoring of its surface properties.[23] Different film compositions can be achieved by using hydrocarbon gases with different hydrogen content. In particular, previous studies[6] showed that hydrocarbon gases with higher fluorine to hydrogen ratio produce fluorocarbon films with lower dielectric constants. With an F:H ratio of 3, CHF3 monomers form fluorocarbons with the lowest reported dielectric constant ($\kappa \sim 2$).[24]

3.2 SURFACE AND BULK CHARACTERIZATION

We annealed the films for 2 hours after deposition at 250 ˚C to minimize surface waviness and improve the final roughness, which was measured by AFM to be ~ 5 Å. This value agrees with roughness measurements on similar fluorocarbon films[23]. We used a Woolam Variable Angle Spectroscopic (VAS) ellipsometer to measure the thickness and optical constants of the fluorocarbon films. Both $\Psi(\lambda)$ and $\Delta(\lambda)$ were acquired over a spectral range of 300 to 1000 nm at 60-70 degree angles of incidence. We fit the data to a Cauchy dispersion model and measured film thicknesses ranging from 8 to 37 nm. The real index of refraction n was relatively uniform over the range of wavelengths investigated and was close to 1.5 as is typical of thin polymer films.[23,25,26] Both n and k show, for films thinner than 25 nm, a thickness dependence that is characteristic of a change in film morphology. For films thinner than 8 nm, ellipsometry measurements failed to generate unique fits and X-ray photoelectron spectroscopy (XPS) was used instead. In this thickness range, the fluorocarbon films are thin enough for the excited electrons to penetrate through and reach out into the detector. These electrons provide an indirect measure of film thickness, which is evaluated as[27]

$$d = \lambda \sin(\theta) \ln\left(\frac{C_f}{C_s} + 1\right). \quad (1)$$

The measured film thickness d is proportional to the electron mean free path λ and has a logarithmic dependence on the ratio of C_f to C_s. For the measured fluorocarbon films, λ is ~3 nm[28] and θ, the X-ray angle of incidence, is set to 90˚. C_f and C_s are the atomic concentrations of the polymer film and Si substrate components respectively. XPS has been used extensively to measure the thickness of sub-10 nm thin films[27] and measurements on fluorocarbon films have also been reported.[29] Using both XPS and spectroscopic ellipsometry, we measured film thicknesses ranging from 2 to 37 nm.

In addition to measuring film thickness, XPS provided a means for determining the chemical composition of the thin films. XPS is able to detect functional groups in the C−F system because of the wide separation (~2 eV) in their binding energies. Table 3.1 shows the different C−F functional groups in terms of binding energies and designations. Both carbon-bonded −C− and hydrogen-bonded −C−H groups have similar binding energies and therefore, they cannot be distinguished by XPS. The measured C1s core level XPS spectra (Fig. 3.1) of the fluorocarbon films show distinct peaks that are characteristic of −C−, −C−CFx−, −CF−, −CF2− and −CF3 functional groups. The percent contribution of each functional group to the total chemical structure of the film depends on film thickness. It is equal to the area under a Gaussian-Lorentzian line shape (70 % Gaussian - 30 % Lorentzian) curve that is fitted to the XPS peak and centered at the binding energy characteristic of the functional group. We evaluated the fluorine to carbon ratio for each thickness of the polymer by multiplying the percent contribution of each functional group by the number of fluorine atoms bonded to the carbon atom forming the group. The ratio is expressed as

$$\frac{F}{C} = \frac{(3\times\%CF_3 + 2\times\%CF_2 + 1\times\%CF)}{100} \tag{2}$$

%CFx (x = 1, 2, 3) corresponds to the percent contribution of group −CFx− to the overall chemical composition of the film as evaluated from the area under the Gaussian Lorentzian curve fits of the −CFx− intensity peaks. We find this ratio to increase with thickness. The fluorine to carbon ratio is 0.65 for a 2 nm film and increases to 1.3 for the thickest film, 37 nm.

TABLE 3.1. Functional groups and corresponding binding energies as identified from a Gaussian-Lorentzian curve fitting of the C1s core level XPS spectra.

Functional Group	Binding Energy[a]
$-\underline{C}-$, $-\underline{C}H-$	285.0
$-\underline{C}-CF_x-$	286.9
$-\underline{C}F-$	288.7
$-\underline{C}F_2-$	291.5
$-\underline{C}F_3-$	293.5

[a] Ref.[26]

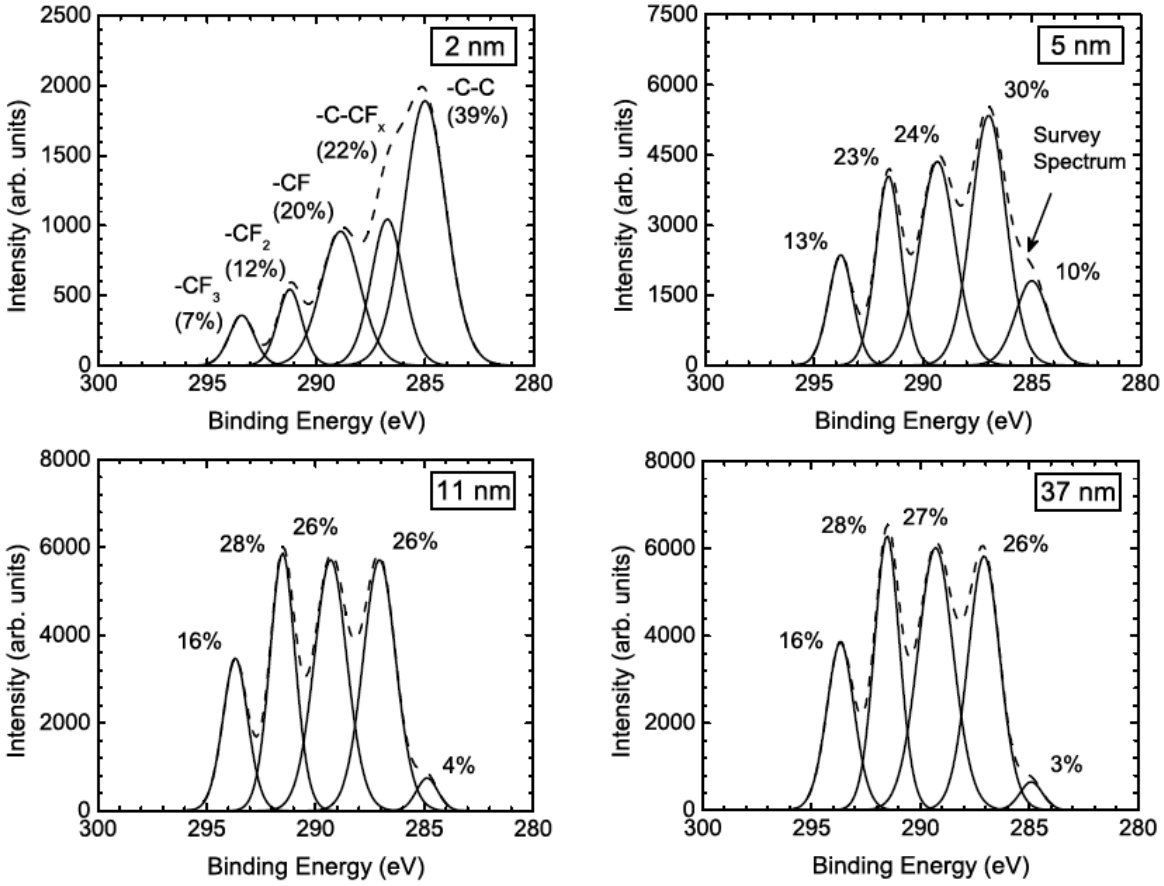


FIGURE 3.1. C1s core-level XPS spectra of the fluorocarbon films showing a change in film composition at different film thickness.

CHAPTER 4

DESIGN AND FABRICATION OF THERMAL CONDUCTIVITY MEASUREMENT PLATFORM

4.1 DESIGN OVERVIEW

For thermal conductivity of single Si nanowire measurement, MEMS platform has been fabricated. Figure 4.1. shows schematic of device design. Basic design has two separated free standing rectangular membranes, lateral supporting beams, and metallic heater lines and contact pads. The dimension of two membranes is 15 μm by 25 μm. The gap between two membranes was kept in 4 μm. The two membranes were initially connected by a bridge with 2 μm width, and the bridge is disconnected by focused ion beam (FIB) with desired gap distance. This process allows us to install nanowire/tube with various lengths from 4 μm up to 0.5 μm. Figure 4.2 shows procedure of creating gap with various lengths. Green color represents two membranes, red color represents heater lines, blue color represents electrode lines which will give electrical contact through nanowire, and black color represents single nanowire. Supporting beams have 2 μm width and 420 μm length. The contact pads are size of 200 μm by 200 μm. The metallic lines connecting contact pads and heater lines have width of 1.5 μm. Lastly, heater lines have 300 nm width and total length has 250 μm. In Appendix A, the details of mask design are reported.

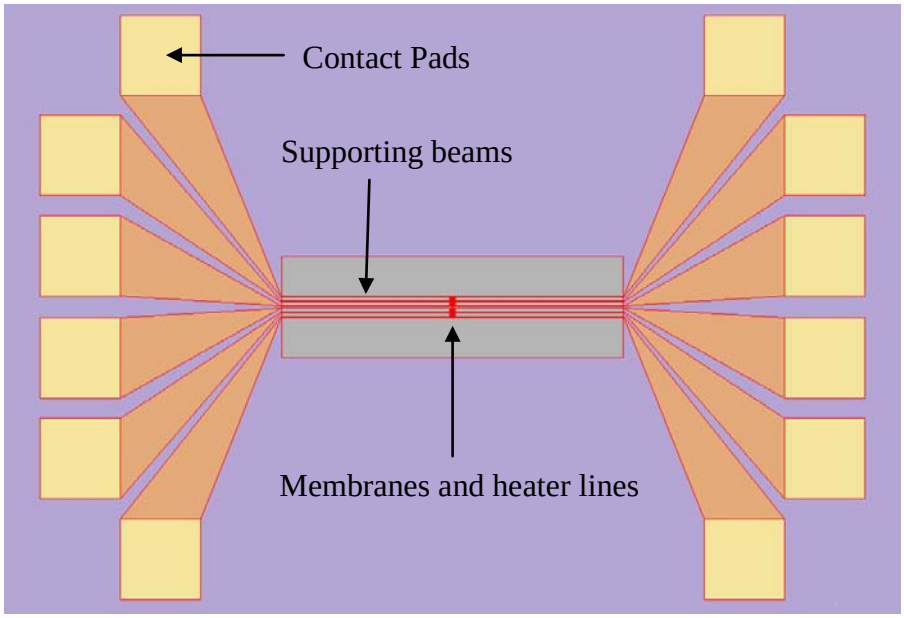


FIGURE 4.1. Schematic of device design.

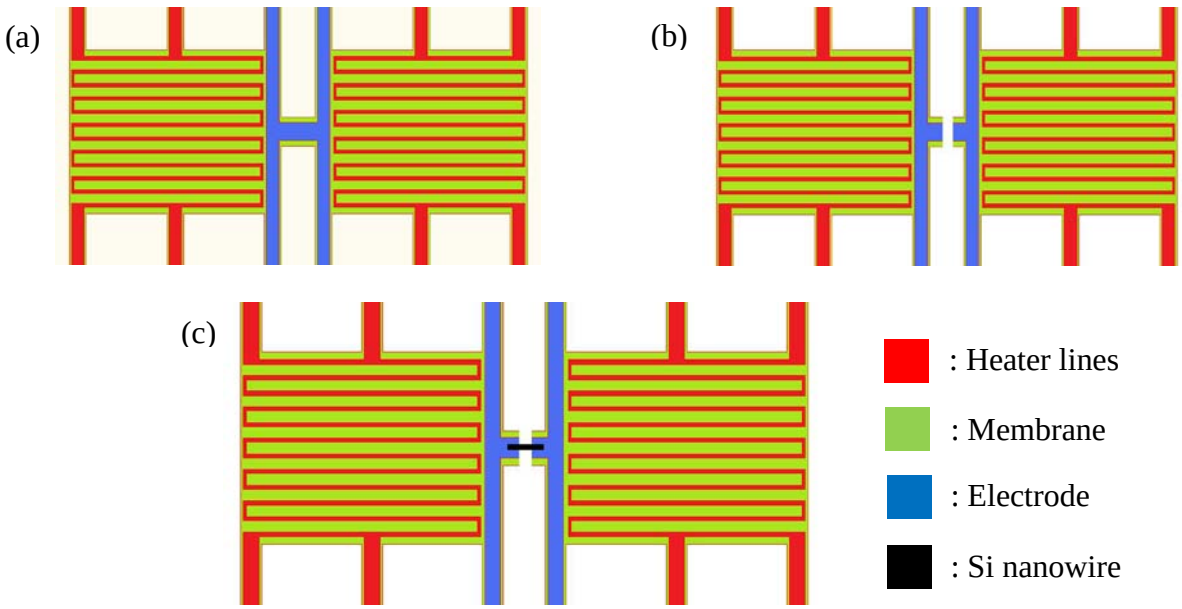


FIGURE 4.2. Fabrication process flow for creating gap with various lengths: (a) membrane is connected by a bridge. (b) bridge is disconnected by FIB. (c) Si nanowire is placed in between two membrane.

4.2 THERMAL CONDUCTANCE ANALYSIS

To verify if sufficient heat is going through the nanowire, we have performed simple thermal conductivity analysis on our design. First, we started with 1-D analysis. Figure 4.3 shows simple thermal circuit diagram for our design. To have sufficient amount of heat flow across the nanowire, thermal resistance of beam structure, R_b, and thermal resistance of nanowire, R_n has to be comparable. Thermal conductance of nanowire with 50 nm diameter and 1 μm length is ranging from 20 to 90 nW/K. In fig. 4.4, we have compared our model with the design of Li Shi et al. Our design comparably has lower conductance at higher temperature regime. However, the thermal conductance is still comparable with thermal conductance of nanowire. Thus, this design is still valid for thermal conductivity measurement.

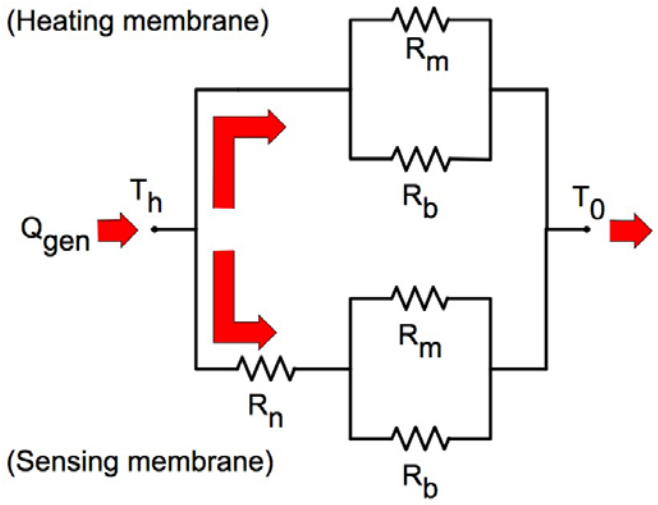


FIGURE 4.3. Schematic of simple thermal circuit diagram of the device.

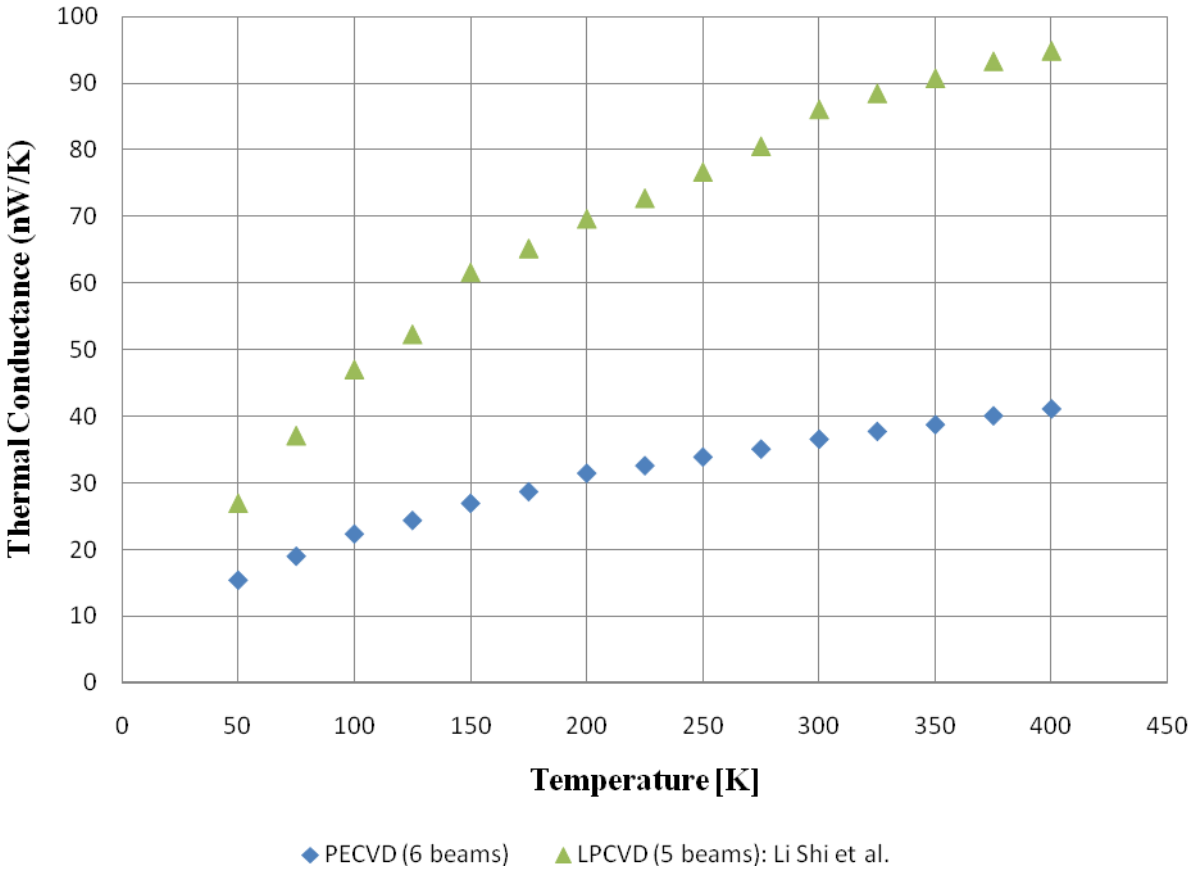


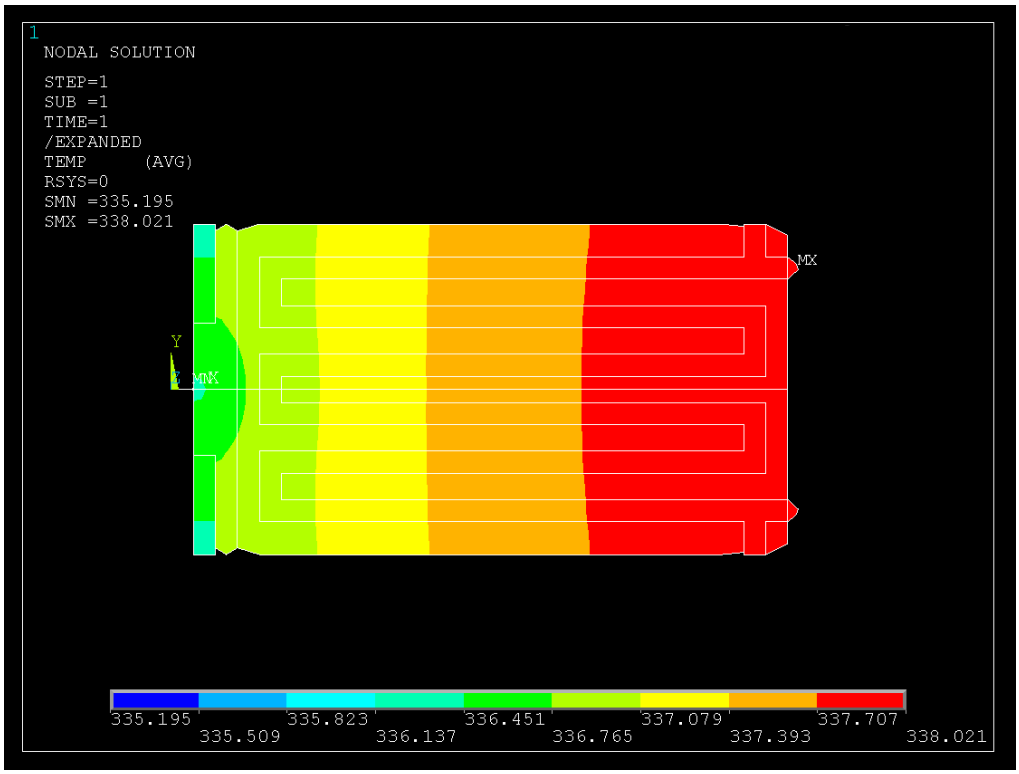
FIGURE 4.4. Plot of thermal conductivity of supporting beam comparing with design of Li Shi et al.

We assume that the temperature distribution of the free standing membrane is uniform over the surface. We have calculated and compared between internal thermal resistance of membrane and supporting beams in order to verify temperature uniformity. For infinitely thin rectangle of length L, width w, and temperature T_1 in an infinite medium of temperature T_2, the internal thermal resistance is expressed as,[37]

$$R = \frac{L_c}{q^*_{ss} k A_s} \quad , where \;\; L_c = \left(A_s / 4\pi\right)^{1/2}, \quad A_s = 2wL, \quad q^*_{ss} = 0.932 \tag{3}$$

The calculation reveals that the internal thermal resistance is 1.1×10^{4} K/W for the membrane and 2.98×10^{7} K/W for the supporting beams. The internal resistance of the membrane is 3 order magnitudes less than thermal resistance of the beam. Thus, we can confidently assume that the temperature distribution of the membrane is uniform. Additionally, we have performed simulation of 2 dimensional temperature distribution of the membrane with finite element method using ANSYS software, and fig. 4.5 shows the result with specific properties of Si nanowire; the diameter is 100 nm, length is 1 μm, and thermal conductivity is 20 W/mK at 300 K. It reveals that there is around 1.2 K difference in temperature distribution across the membrane while temperature gradient across the Si nanowire is 15 K. Comparing to overall temperature raise in the membrane, the temperature difference across the membrane is negligible.

(a)



(b)

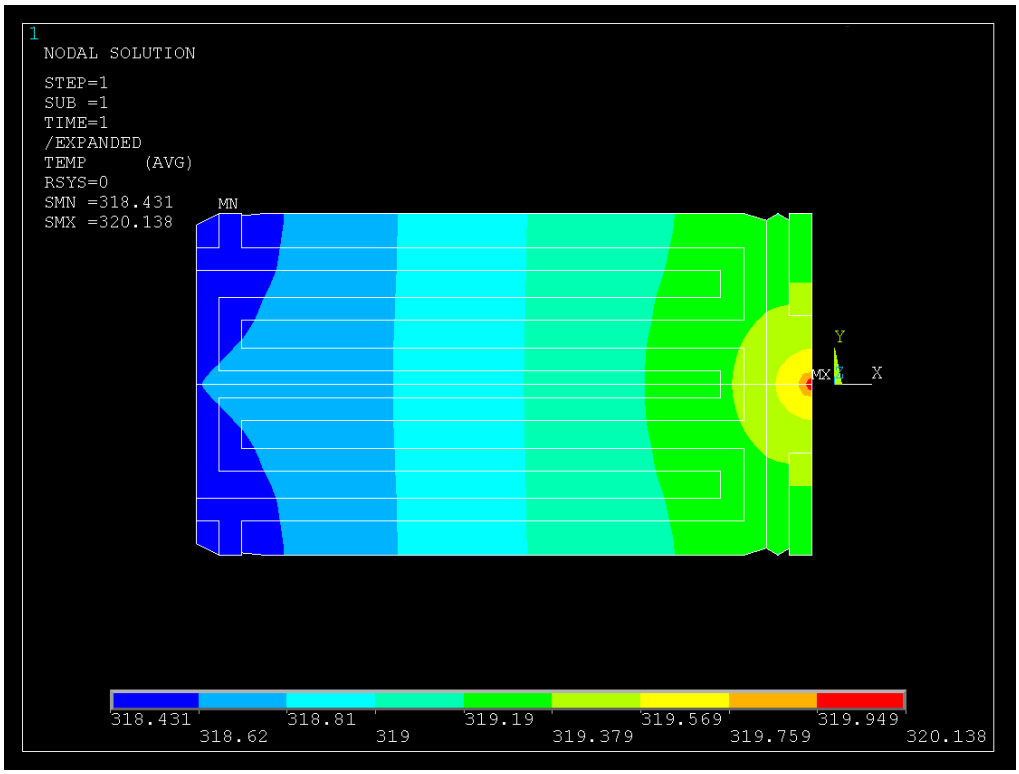


FIGURE 4.5. ANSYS 2D temperature distribution analysis of (a) heating membrane and (b) sensing membrane at 300K.

4.3 FILM STRESS ANALYSIS

We have faced on problem regarding film stress problem during the fabrication. The free standing structures were broken after the releasing process. The curvatures of the broken beams indicate that the structures having compressive stress. Based on measurement of single layer's film stress, we find that current design has high compressive stress, -250 MPa. Thus, three different methods are suggested. Method 1 is using only PECVD SiN_x with mixed frequency (M.F.) RF power, which gives very low stress, while its total thickness keeps in 600nm. Method 2 is keeping every layers same but reducing thickness of PECVD SiO_2. It reduces total film stress, because PECVD SiO_2 has high compressive stress. Last method is using PECVD SiN_x with high frequency (H.F.) RF power, which has high tensile stress. This reduces total stress by canceling stresses between tensile stress and compressive stress.

TABLE 4.1. Summary of film stress analysis

		Method 1	Method 2	Method 3	Broken Sample
1st Layer	Film	PECVD SiN_x (M.F.)	PECVD SiN_x (M.F.)	PECVD SiN_x (H.F.)	PECVD SiN_x (M.F.)
	Thickness [nm]	349	522	506	500
	Stress [MPa]	-23	-24	451	-24
2nd Layer	Film	Pt	Pt	Pt	Pt
	Thickness [nm]	30	30	30	30
	Stress [MPa]	1009	1047	971	1009
3rd Layer	Film	PECVD SiN_x (M.F.)	PECVD SiO_2	PECVD SiO_2	PECVD SiO_2
	Thickness [nm]	300	100	300	300
	Est. Stress [MPa]	-23	-750	-750	-750
Est. Total Stress [MPa]		**43**	**28**	**39**	**-250**

4.4 FABRICATION USING E-BEAM LITHOGRAPHY AND TMAH ETCHING

To define sub-micron patterning and releasing structure to free standing, two different design and methods has been tried. First, we have fabricated this structure using E-beam lithography to define 300nm width of metallic heater lines and TMAH wet etching to releasing the structures. We started with 2" <100> Si wafer because of limited number of pattering due to E-beam lithography process. We deposited 500nm PECVD SiN_x film, which is going to be a base body of free standing structures. When we deposit the SiN_x film, we used low stress recipe, which uses mixed frequency RF power. On top of SiN_x film, we deposited 3nm Ti film and 30nm Pt film using E-beam evaporator with deposition rate of 0.3 Å/sec and 2 Å/sec respectively. Pt film is going to be metallic heater lines and contact pads, which will be sitting onto free standing SiN_x membrane. Ti film was deposited for adhesion layer between SiN_x and Pt film. Then, we spun PMMA on the substrate with around 400nm thickness, and 300nm heater lines, contact pads, and electrodes are patterned by E-beam lithography. Then, we deposited 50nm Al film using E-beam evaporator with deposition rate of 2 Å/sec. This Al film is for mask material during the ion milling process which will be followed. By liftoff process, heater line patterns are transferred to Al film. Ion milling was used to pattern Pt while Al patterns become a mask. For the ion milling, we used reactive ion etching system (RIE) with 10 sccm of Ar flow rate, 35 mTorr of chamber pressure, and 300 W of RF power. Etch rate for Pt was measured and etch rate is 8.5 Å/min. After Pt patterning, Al patterns were removed by *type A aluminum etchant* for 1 min. Then, we deposited 300nm PECVD SiO_2 for thermal and electrical insulator. Optical photolithography was used to define supporting beam structure and two membranes. We used Shipley 1813 positive resist with 150 mJ/cm^2 of UV exposure using I-line aligner (Quintel) and MF 319 developer for 18 seconds. After PR patterning, we hard-baked PR at 125°C for 5min.

Using Freon RIE, PR patterns are transferred to SiO_2 layer and SiN_x layer by etching them using CF_4 gas. Then, we etched SiO_2 layer with photolithography and HF wet etching only where contact pads and electrodes are located because we need electrical contact to metallic contact pads and electrodes for nanowire. The device was diced using disco dicing saw into 9mm by 9mm size. Figure 4.6 shows SEM image of completed device before releasing step. Finally, the structure was released using 25 % TMAH wet etching for 6 hours. TMAH etching was done from the top Si exposure region and it continuously etching Si until it makes around 100 μm deep trench underneath the structure.

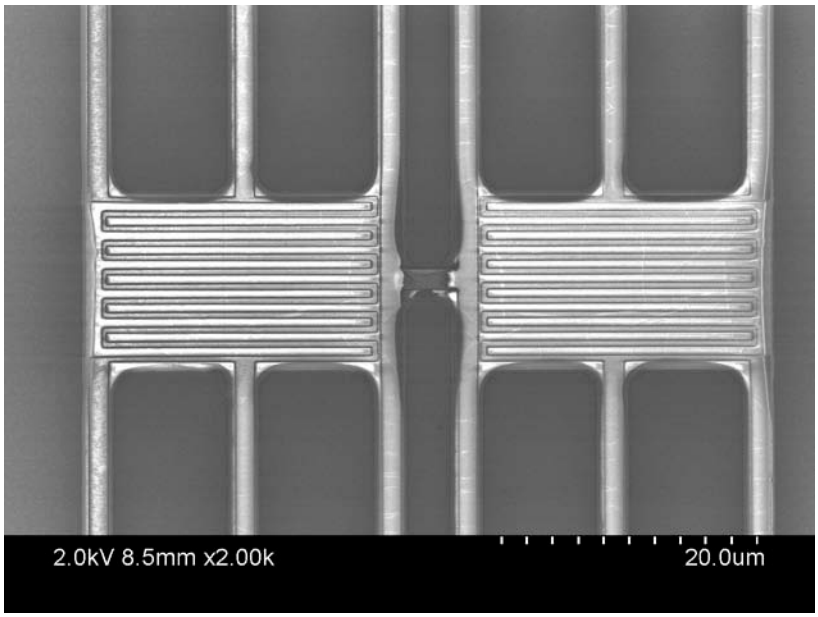


FIGURE 4.6. SEM images of structures before releasing step.

4.5 PROBLEMS AND TRIAL SOLUTIONS

We had faced three problems when we used E-beam lithography and TMAH wet etching process. First, we designed photo-mask for opening contact pads as exact size of contact pads. This caused etching not only to surrounding SiO_2 layer but also over-etching SiN_x underneath contact pads due to its misalignment. Thus, Si underneath the contact pads were etched during TMAH etching, because SiN_x layer was over-etched and it allows TMAH goes inside of Si. Figure 4.7 shows defects on contact pads. Second problem is stiction problem after TMAH wet etching. Since the supporting beams are long and narrow, stiction between adjacent beams was inevitable. Figure 4.8 shows a stiction between the beams after TMAH wet etching. Lastly, E-beam lithography process is unfavorable, because it is too slow and expensive and the yield was less than 50 %.

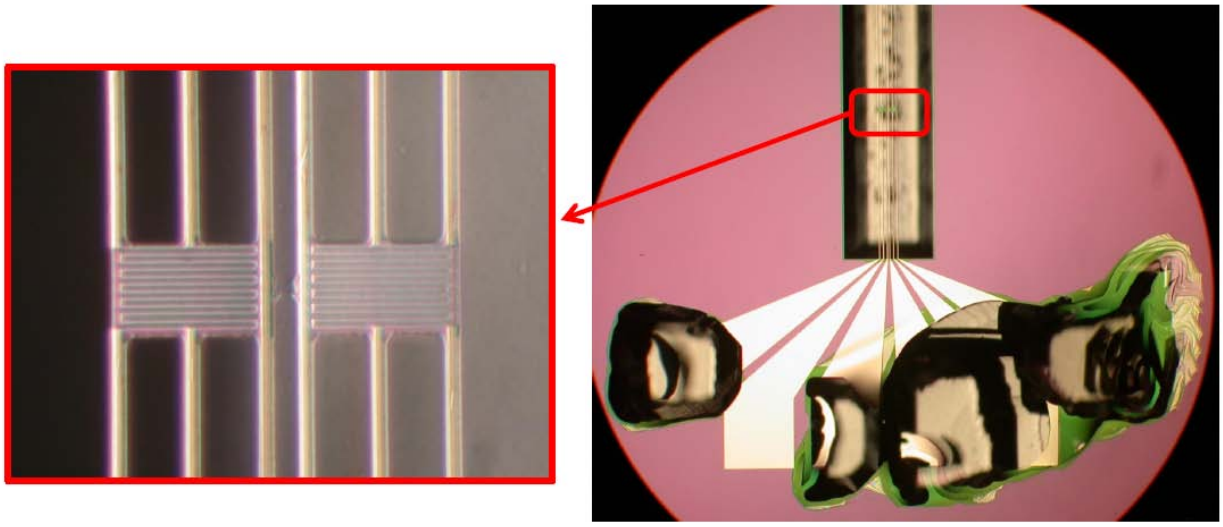


FIGURE 4.7. Free standing membranes and defects in contact pads.

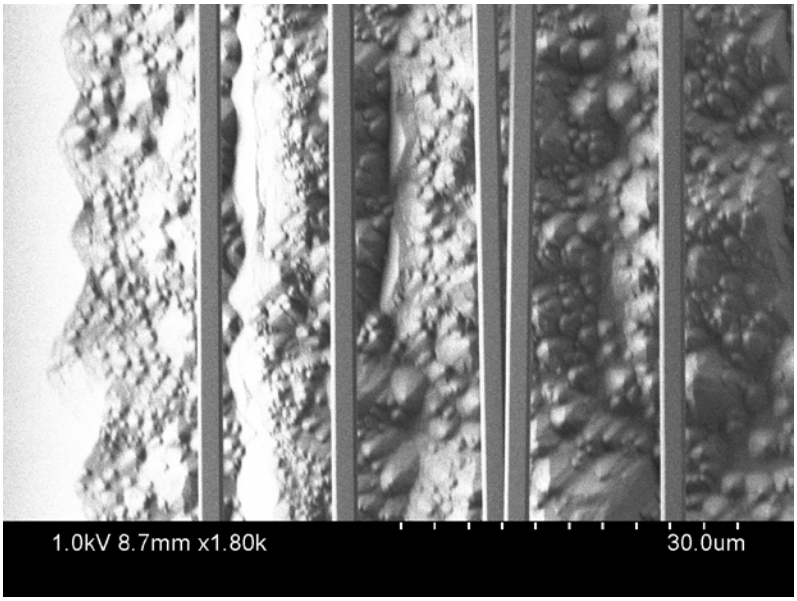


FIGURE 4.8. Example of stiction problems.

To overcome those problems, we modified design and fabrication processes. First, we reduce the size of contact pads with 50 μm less to give more tolerance on alignment. Also, we used RIE dry etching instead of HF etching, since dry etching is more directional and reliable. Second, for releasing process, we used XeF_2 etching instead of TMAH wet etching. XeF_2 etching has selectivity between Si and SiO_2 or SiN_x with 1 to infinity, and also it is vapor etching system which does not make stiction problem. For another solution for stiction problem, we designed spacers between adjacent beams. Lastly, we used combination of optical photolithography and oxygen plasma etching to pattern 300 nm heater lines instead of E-beam lithography. Figure 4.9 shows the result of oxygen plasma etching to reduce the width of Shipley 1813 resist line. During 10 minutes of etching with 300W RF power, 5 sccm O_2 flow rate, and 500mTorr pressure at room temperature, the line was reduced from 3.1 μm to 2.8 μm. These modifications have been applied and solved most problems that we have been faced.

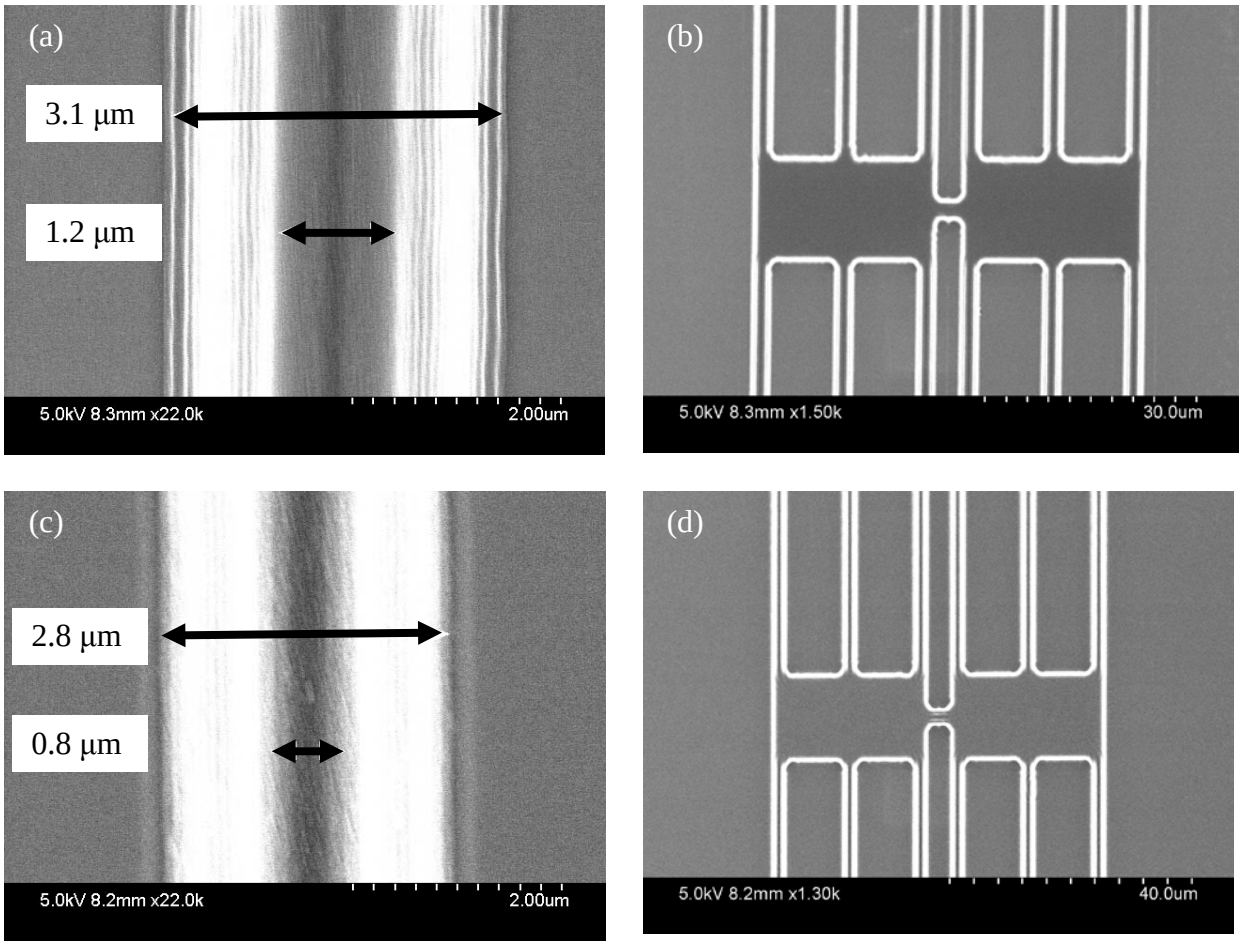


FIGURE 4.9. O_2 plasma etching of AZ 5214 patterns: (a), (b) before etching (c), (d) after 10 minutes etching.

4.6 FABRICATION USING OPTICAL LITHOGRAPHY AND XeF_2 ETCHING

We have fabricated 300nm Pt heater lines using optical lithography with oxygen plasma etching technique. On top of the 30nm Pt film, 100nm PECVD SiO_2 film was deposited for the etch mask during the ion milling process. Then, we first patterned the heater lines with 1 μm width using optical lithography. AZ 5214 positive resist was spun on the substrate at 5000 rpm for 30 second. Then, the resist was post-baked at 110 C for 1 minute. Then, the resist was exposure to UV source (I-Line) using aligner (Quintel) with vacuum mode for 112.5 mJ/cm^2. MF

319 was used to develop the resist for around 28 second. 1μm lines in the mask design produce around 1.5 μm lines through the optical lithography. The resist patterns were etched isotropically by oxygen plasma etching for 30 minutes, which reduced width of the 1.5 μm lines to 300nm lines. Then, PECVD SiO_2 layer was patterned using Freon RIE with CF_4 gas. Lastly, Pt film was patterned using ion milling for 35 min at 10 sccm of Ar flow rate, 35 mTorr of chamber pressure, and 300 W of RF power. Figure 4.10 show the result of heater line patterning with 300nm width using optical lithography.

We have used XeF_2 etching system to release the structures to free standing. This method does not make stiction problems, because it is vapor etching system. The Si was etched under 3 Torr pressure for 5 minutes (5 cycles). Etch rate is known to be 2 μm/min. Figure 4.11 shows free standing structures made by XeF_2 etching. This testing sample was only nitride and oxide layers without metallic lines. We can conclude that the structure is completely released, because the SEM images are clearly showing the underground textures through the membrane. However, some of the structures have been broken during the XeF_2 etching, and the curvature of the broken structures proves that the failure has been occurred due to high compressive stresses. Figure 4.12 shows the condition of the broken structures after XeF_2 etching. For the solution of this stress problem, three different methods have been addressed from section 4.3.

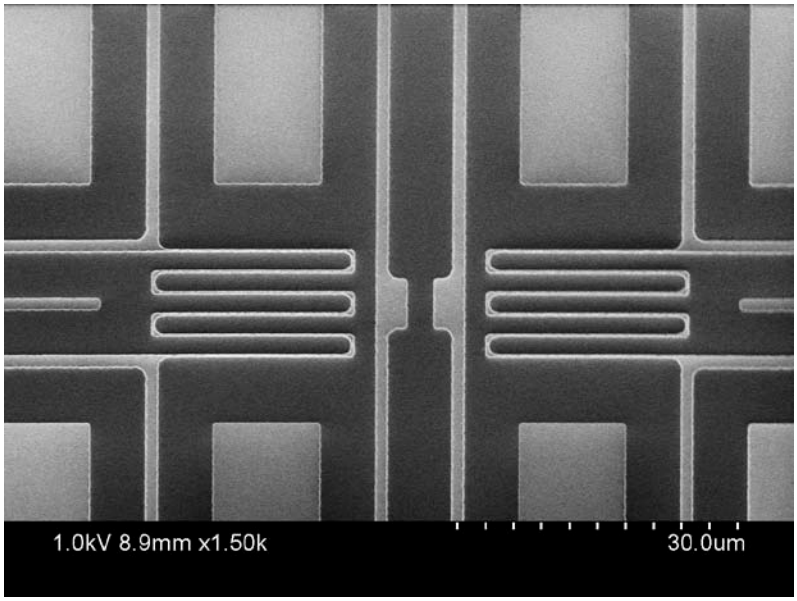


FIGURE 4.10. 300nm Pt heater lines done by optical lithography.

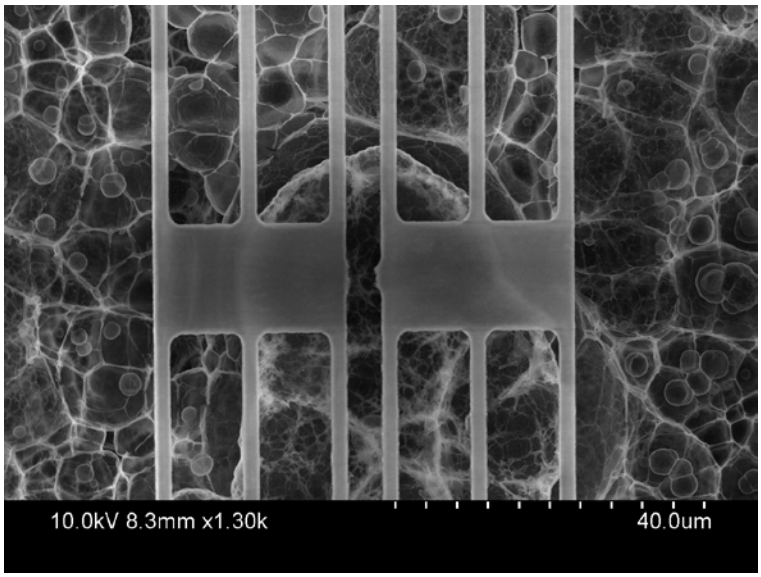


FIGURE 4.11. Free standing structure done by XeF_2 etching.

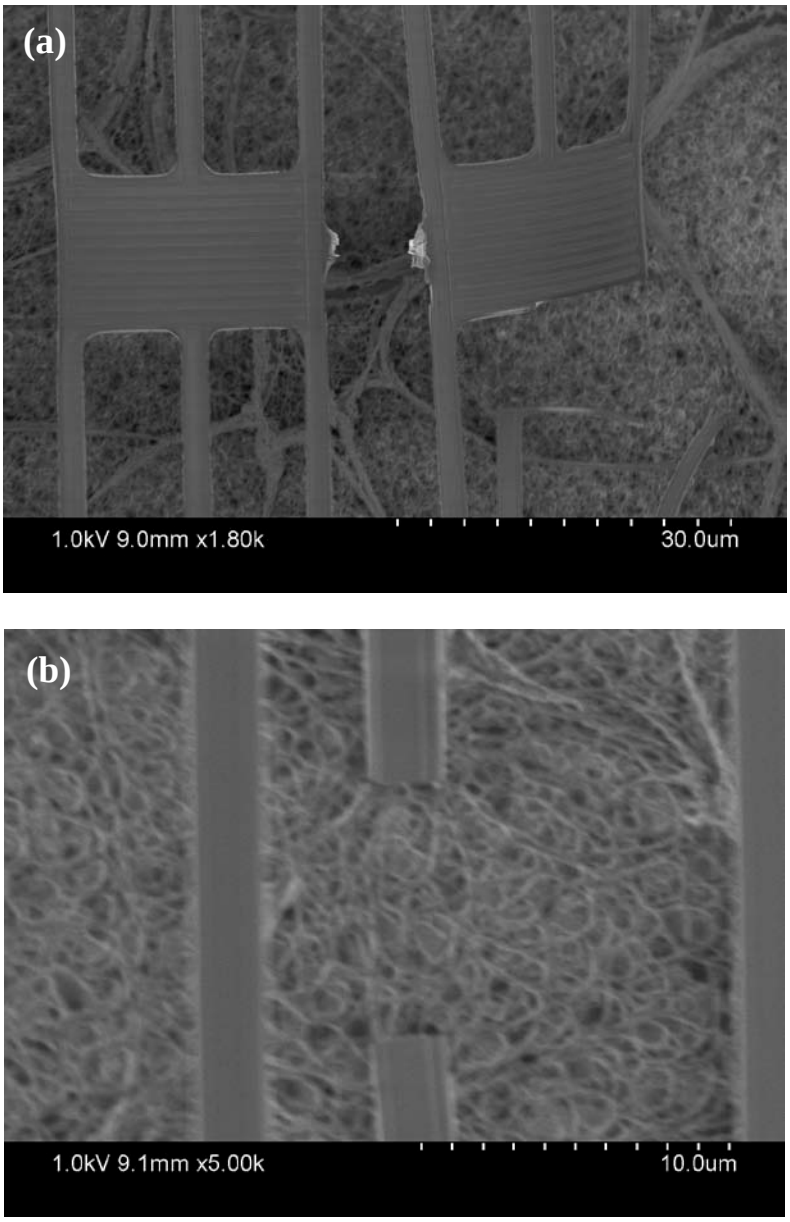


FIGURE 4.12. Broken free standing structures due to the film stress.

CHAPTER 5

METALLIC GRATINGS FOR GENERATING GHz SURFACE PHONONS

5.1 FABRICATION OF ALUMINUM GRATINGS

We fabricated aluminum grating structure using e-beam lithography and liftoff technique. First, we spun poly methyl methacrylate (PMMA) onto silicon substrate with 400 nm thickness. Then, we patterned grating structures using e-beam lithography (JEOL JBX-6000FS Electron Beam Lithography System). The grating structure has around 140 nm width and 320 nm period. Then, we deposited 50nm aluminum film onto patterned surface and liftoff PMMA patterns. Finally, 50nm height and 180 nm width of aluminum grating structures remain with 320 nm period. Figure 5.1 shows fabricated aluminum grating structure images inspected by scanning electron microscope (SEM).

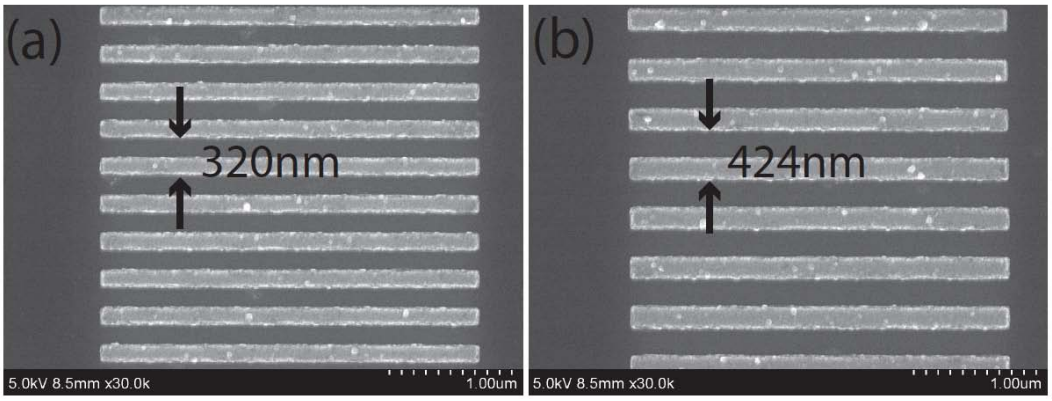


FIGURE 5.1. SEM images of aluminum gratings.

5.2 GENERATING GHz SURFACE PHONONS

We use picosecond pump-and-probe optical measurement to generate and detect SAW.[30,31] Figure 5.2 shows diagram of a pump-and-probe system used in our work. Picosecond pump-and-probe optical measurement uses two separate laser pulses, pump beam and probe beam, which originate from same short pulse laser system. We use Ti: Sapphire laser system with 785 nm of wavelength, 25 mW of total laser power, 80.6 MHz of repetition rate, and 100 fs rise time. Pump beam generates SAW by focusing laser pulse onto small spot on aluminum grating structures and generating periodically varying thermal expansion. Probe beam detects SAW by collecting data of reflectivity changes in time. Mechanical delay stage makes pump beam travels longer distance than probe beam so that pump beam and probe beam cannot reach the sample at the same time. Photodiode detector collects reflected probe beam from the sample and connected lock-in amplifier measures reflectivity changes in time. Electro-optic modulator and polarizer prevent pump beam to be collected through photodiode detector.

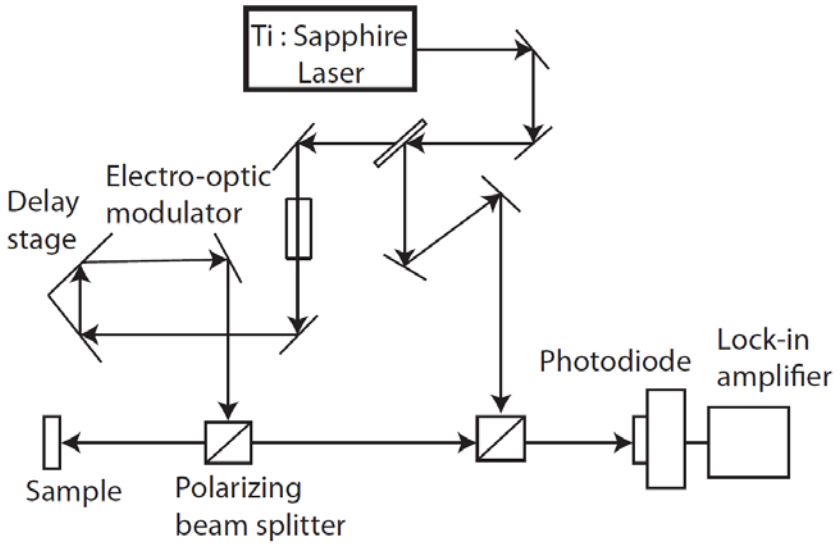


FIGURE 5.2. Diagram of pump-and-probe system.

The pump-and-probe system measures change of reflectivity on sample surface due to SAW. In-phase voltage signal of lock-in amplifier, which is connected with photodiode detector, gives you relative change of reflectivity, ΔR.[32] We fabricate four grating samples with different width of grating but same grating period, 320 nm and 424 nm, by changing dose intensity during e-beam lithography. Figure 5.3 (a) shows relative reflectivity changes in function of delayed time of pump beam for the sample of 424 nm in period and 290 nm in width. The change of reflectivity behaves decaying and oscillating as delayed time increasing. This oscillation is due to SAW, but decaying behavior is due to thermal effect by heating and rapid cooling by short laser pulse. This thermal background has been removed since we are only interested in SAW signal. Figure 5.3 (b) shows relative reflectivity changes which thermal background is removed by filter. Fourier transform of this graph into frequency domain gives actual frequency of SAW signal. Figure 5.4 shows fast Fourier transform results of each grating samples. We expect the frequency of SAW, $\omega = VR/p$, where VR and p is Rayleigh velocity and period of grating respectively[31]. Both 320 nm and 424 nm period sample has the highest peak at 15.6 GHz and 11.7 GHz. We consider these frequencies as SAW frequency while the theoretical values are 14.7 GHz and 11.1 GHz for 320 nm and 424 nm period sample respectively. Thus the results agree with theoretical values closely. We observe there are changes in power of Fourier transform but no change in peak frequency.

The generation of surface acoustic waves in nanostructure-on-substrate can be studied using the theory of thermoelasticity. The differential absorption of laser pulse in the grating and the substrate sets up a periodic thermal field at the surface of the substrate which in turn relaxes as an acoustic wave. Thus the key parameters that affect the frequency and the power of SAW mode are the period of the grating (p) and the duty cycle of the grating ($\eta = w/p$). The frequency

of the SAW is a strict function of the period of the grating while the power of the wave depends on the duty cycle and the period. The power of SAW can be enhanced with decreasing period but the attenuation of the SAW increases with this decrease. Hence it is important to increase the efficiency of SAW generation for a given period of grating by varying the duty cycle of the grating. In Fig 5.5, it can be seen that power of SAW mode decrease with increase in the duty cycle.

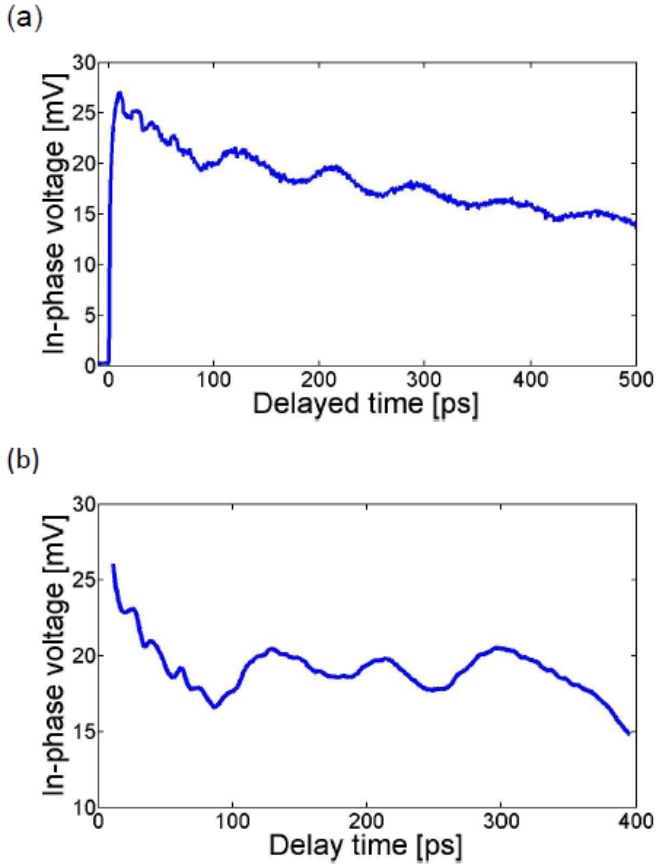


FIGURE 5.3. (a) Relative change of reflectivity in function of delay time for grating with 424 nm period and 290 nm grating width. (b) Relative change of reflectivity which thermal background is removed by filter.

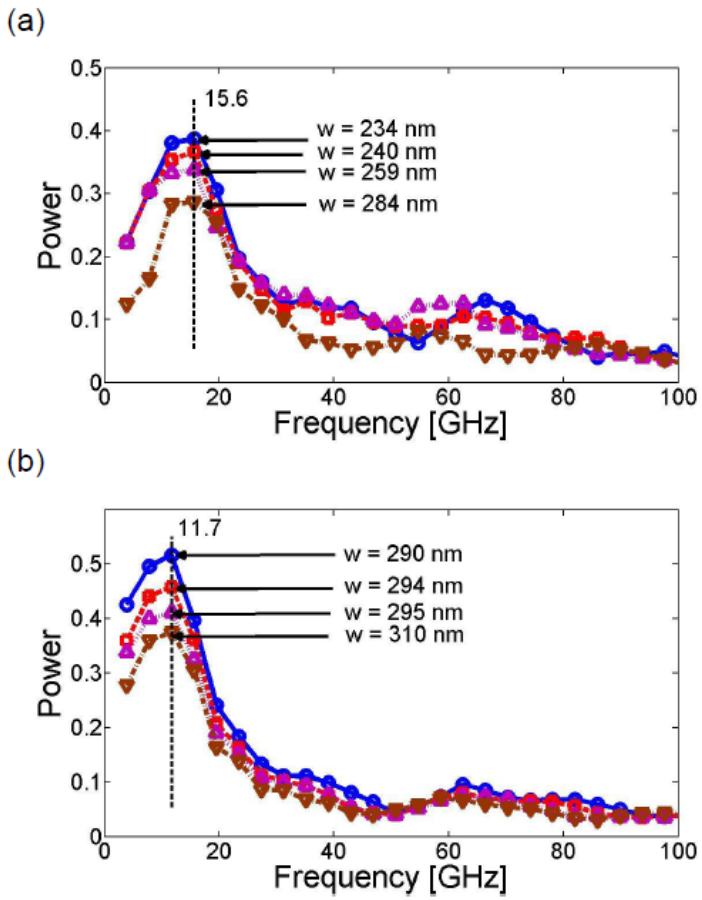


FIGURE 5.4. Power of Fourier transform in frequency domain for (a) 320 nm grating period and (b) 424 nm grating period with different aluminum width.

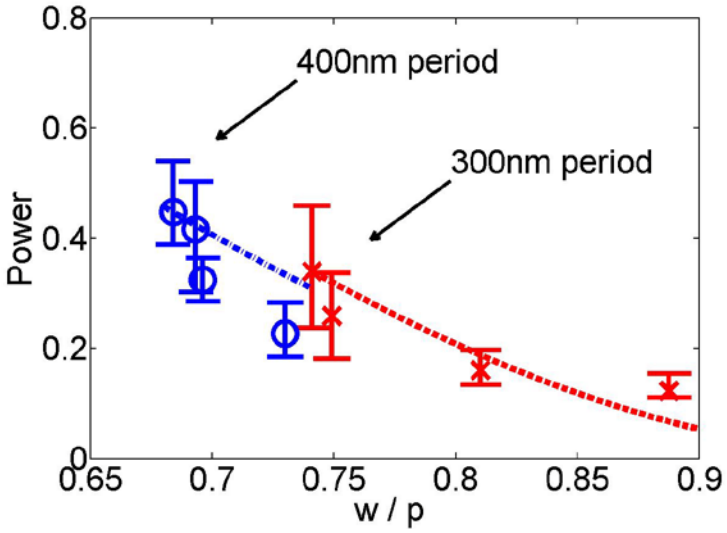


FIGURE 5.5. Power of the highest peak from Fourier transform in function of ratio of grating width to grating period.

CHAPTER 6

SUMMARY

In summary, first, we have successfully fabricated ultra-thin fluorocarbon polymer film thickness range ranging from 6nm to 33nm using plasma polymerization with CHF_3. This uniform ultra-thin film can be used to study thermal transport theory in ultra-thin polymer film. Also, these polymers can be also used in other applications, such as heat storage material or coating material in MEMS fabrication. Second, we have fabricated MEMS platform for thermal conductivity measurement of single nanowire. We have successfully resolve problems regarding releasing the free standing structure and stiction problems. However, we have faced film stress problems. We suggest three different solutions to resolve this issue by changing layer thickness and types of layer. Lastly, we have fabricated metallic grating lines and successfully generated SAW using picosecond acoustics. When a ultra-short pulse laser is incident on a nanostructure grating on a substrate, the differential absorption of pulse in grating and substrate sets up a periodic thermal field at the surface of the substrate. This periodic thermal stress launches a SAW with the same frequency as that of the thermal filed. Experimental frequency of SAW agrees with theoretical value which depends on period of gratings and velocity of SAW. We prove that the power of SAW generated in this process is a function of duty cycle of the grating. It has been shown that the efficient generation of the SAW is obtained at a duty cycle of $\eta=0.5$ while increasing the duty cycle beyond it will lead to decay in the power of surface acoustic wave. Our experimental results also show that the mass loading effect on the frequency of SAW due to the grating is negligible for Aluminum grating.

REFERENCES

[1] R. S. Prasher et al., J. of Heat Transfer, **125** (6), 1170-1177 (2003).

[2] J. A. Forrest, and K. Dalnoki-Veress, Adv. in Coll. and Interface Science, **94**, 167 (2001).

[3] C. L. Soles et al., Phys. Rev. Lett. **88**, 037401 (2002).

[4] K. Kurabayashi et al., IEEE J. Micro. Sys., **8** (2), (1999).

[5] P. B. Kaul, K. A. Day, and A. R. Abramson, J. Appl. Phys., **101**, 083507 (2007).

[6] J. A. Theil, J. Vac. Sci. Technol. B **17**, 2397 (1999).

[7] E. Ruckenstein and S. V. Gourisankar, Biomaterials, **7**, 403 (1986).

[8] D. Koshel et al., Surf. Coat. Technol., **173**, 161 (2003).

[9] F. J. DiSalvo, et al, Science **285,** 703 (1999).

[10] A. I. Boukai et al., Nature, **451**, 7175 (2008).

[11] L. Shi et al., Journal of Heat Transfer, **125**, 881 (2003).

[12] M. Tonouchi, "Cutting-edge terahertz technolog", Nature photonics, 1, (2007).

[13] M. Nagel, H. Kurz, J. Phys, Condens. Matter, **18,** (2006).

[14] B. Luthi, "Physical Acoustics in the Solid State", 2nd ed., Springer, Berlin, (2007).

[15] I. Hosako, N. Sekine, Proceedings of the IEEE, **95** (8), August 2007.

[16] V. K. Varadan, et al., Sensors and Actuators A: Physical, **90**, Issues 1-2, 7-19, May (2001).

[17] E. H. Jacobsen, J. Acoust. Soc. Am., **32**, 949, (1960).

[18] C. Thomsen, H.T. Grahn, H. J. Maris, J. Tauc, Phys. Rev. B, **34**, (1986).

[19] A. G. Antonelli and H. Maris, Physica B **316**, 377-379, (2002).

[20] D. H. Hurley and K. L. Telschow, Physical Review B, **66**, 153301, (2002).

[21] K M. E. Siemens, et al., Appl. Phys. lett. **94**, 093103, (2009).

[22] E. Kay and A. Dilks, J. Vac. Sci. Technol., **18**, 1 (1981).

[23] T. Easwarakhanthan *et al.*, J. Vac. Sci. Technol., **24**, 1036 (2006).

[24] E. J. Winder and K. K. Gleason, J. Appl. Polym. Sci., **78**, 842 (2000).

[25] P. D. Keathley and J. T. Hastingsa, J. Vac. Sci. Technol. B, **26**, 2473 (2008).

[26] S. Tajima and K. Komvopoulos, J. Phys. Chem., **111**, 4358 (2007).

[27] Z. H. Lu and J. P. McCaffrey, Appl. Phys. Lett, **71**, 2764 (1997).

[28] C. D. Bain and G. M. Whitesides, J. Phys. Chem., **93**, 1670 (1989).

[29] N. R. Rueger et al., J. Vac. Sci. Technol. A, **15**, 1881 (1997).

[30] S. Capinski and H. Maris, Rev. Sci. Instrum., **67** (8), August (1996).

[31] T. Lee and G. Cahill, Physical Review B, **71**, 144106, (2005).

[32] D. G. Cahill, Review of Scientific Instruments, **75** (12), December (2004).

[33] J. M. Torkelson et al., Polymer Engineering and Science, **38**, 12, (1998).

[34] K. Koumoto et al., Langmuir, **20**, 3278-3283, (2004).

[35] J. Bougdira et al., J. Vac. Sci. Technol. A, **24**, 4, (2006) .

[36] L. Shi et al., Appl. Phys. Lett, **77**, 26, (2000) .

[37] F. P. Incropera, Fundamentals of Heat and Mass Transfer, p210, John Willey & Sons, New York, (2002) .

[38] M. Ghossoub, *Thermal transport in ultrathin fluoropolymer films*, Master Dissertation, University of Illinois at Urbana-Champaign, Illinois, (2009) .

[39] J. Sadhu, *Photoexcited Hypersonic Surface Acoustic Waves Propagating under Periodic Metal Grating* , Master Dissertation, University of Illinois at Urbana-Champaign, Illinois, (2010) .

APPENDIX A. MASK DESIGN

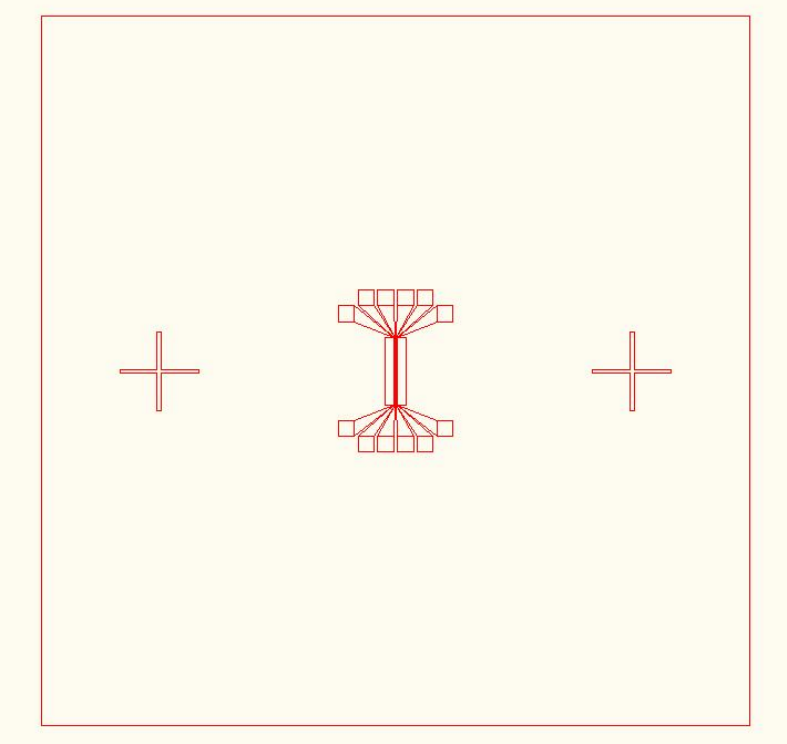


FIGURE A.1. Overlapping all mask designs of one device.

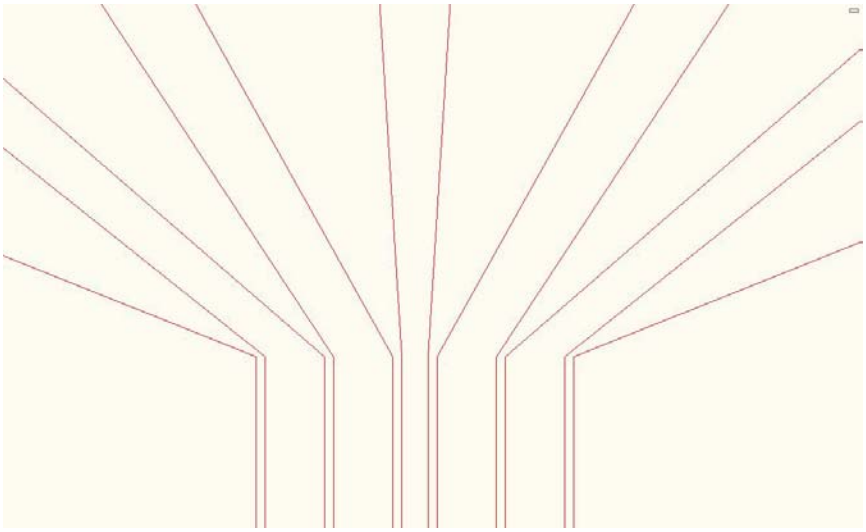


FIGURE A.2. Mask design of interconnection between heater lines and contact pads.

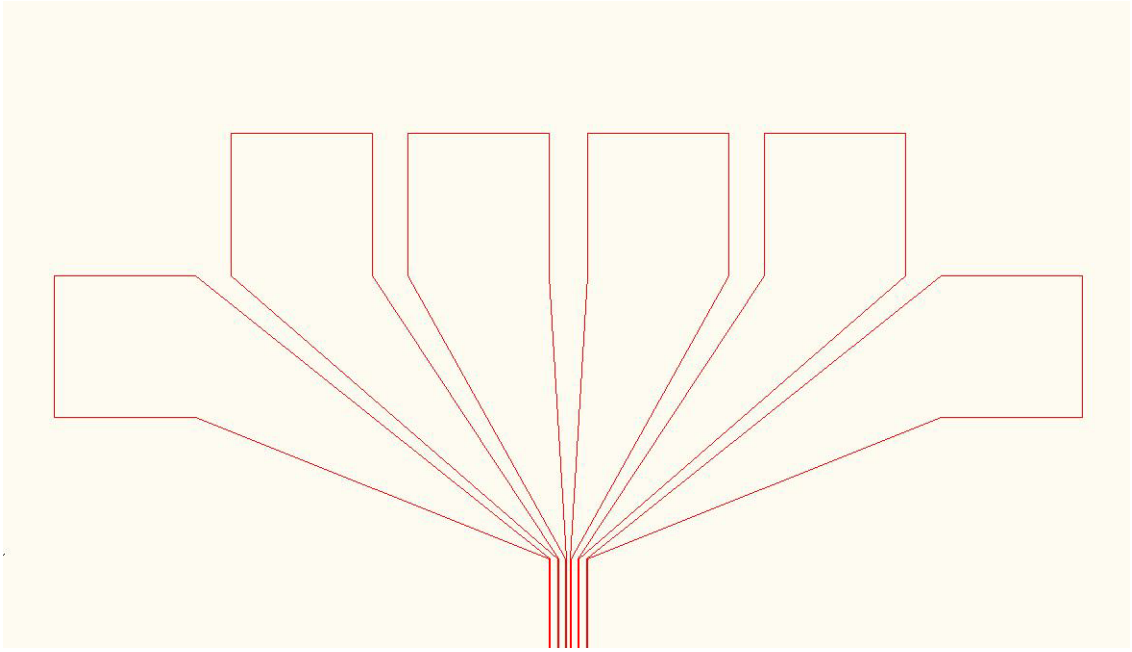


FIGURE A.3. Mask design of contact pads.

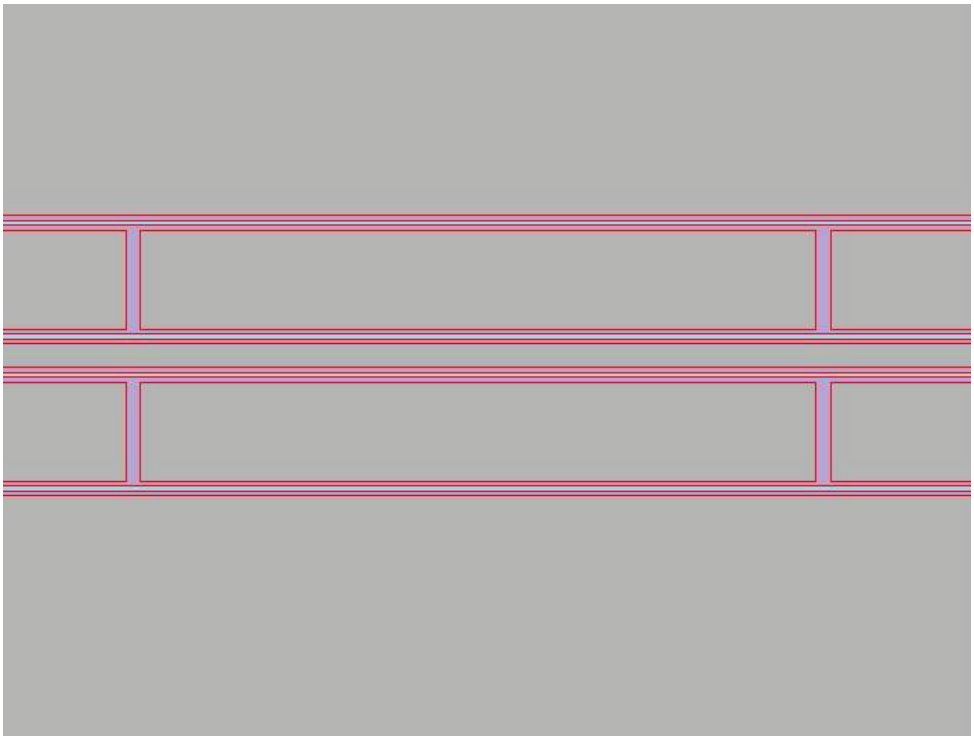


FIGURE A.4. Example of the spacers.

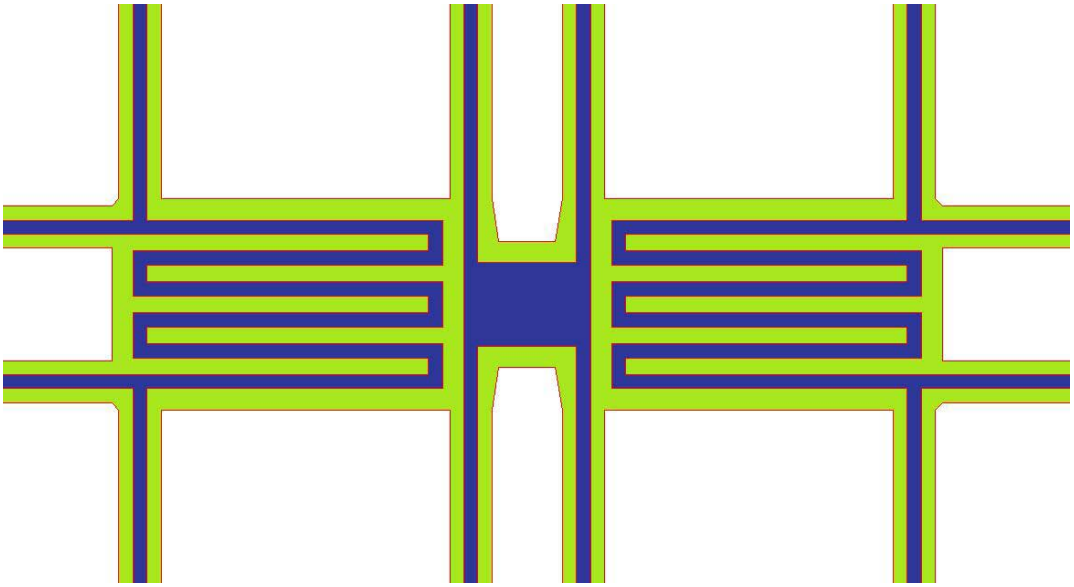


FIGURE A.5. Mask design of modified heater lines with 1μm width.

APPENDIX B. ANSYS ANALYSIS CODE

```
/clear,nostart
/prep7
et,1,plane55
L_nw=2   ! Length of nanowire is 2 micron
D_nw=0.1 ! Diameter is 100 nm
W_b=2    !
!W_Pt=1
W_pl=9
W_PLT=6 ! Width of plate
Ls=2    ! Length of nanowire
t_Pt=0.3
L_Pt=21

ok=(W_b-t_Pt)/2

tv=0.7
Lb=420
Lcoil=252

! INPUT
tSiN=0.5
tPt=0.03
tSiO=0.3
Lnw=1
Dnw=0.02
knw=1
Gc=80e-9
R=Lnw*4/(knw*3.142*Dnw*Dnw*1e-6)+1/Gc
keqnw=Ls/(R*3.142*D_nw*D_nw*1e-6/4)
keqnw=keqnw*1e-6*2/D_nw
Tamb=300
jyo=5.5*tv+5*t_Pt
Wm=2*(jyo+t_Pt/2+W_b/2)
Lm=3*ok+L_Pt+3*t_Pt

! MATERIAL PROPERTIES
mp,kxx,1,1e-6*(tSiN/6+0.2*tSiO)/((tSiN+tSiO)*(tSiN+tSiO)),1e-6*(0.015*tSiN/6+3e-
3*tSiO)/((tSiN+tSiO)*(tSiN+tSiO))
co1=0.015*tSiN/6+tPt*2.45e-8/(7.2*1e-10*300+2.4e-7)+tSiO*3e-3
co2=tSiN/6+0.2*tSiO
mp,kxx,2,1e-6*co2/((tSiN+tSiO+tPt)*(tSiN+tSiO+tPt)),1e-
6*co1/((tSiN+tSiO+tPt)*(tSiN+tSiO+tPt))  ! Oxide,SiN composite
```

```
mp,kxx,3,keqnw                                                    ! Nanowire material

mp,kxx,4,1e-6*co2/((tSiN+tSiO+tPt)*(tSiN+tSiO+tPt)),1e-
6*co1/((tSiN+tSiO+tPt)*(tSiN+tSiO+tPt))  ! Pt,oxide,SiN composite

! Geometry

blc4,-Ls/2,0,(Ls)/2,D_nw/2


blc4,-Ls/2-Lm+ok,jyo,L_Pt+2*t_Pt,t_Pt
agen,6,2,,,,-tv-t_Pt,
blc4,-Ls/2-Lm+ok,0,t_Pt,tv/2
blc4,-Ls/2-Lm+ok,tv*1.5+2*t_Pt,t_Pt,tv

agen,2,9,,,,2*t_Pt+2*tv
blc4, -Ls/2-Lm+ok+t_Pt+L_Pt,tv/2+t_Pt,t_Pt,tv
agen,3,11,,,,2*t_Pt+2*tv
blc4,-Ls/2-Lm+ok,jyo,-2,t_Pt   ! Pt coil

blc4,-Ls/2-Lm+ok-2,jyo+t_Pt/2-0.9,-Lb-ok+2,1.8   ! Change the height as you want
blc4,-Ls/2-Lm+ok-t_Pt/2,jyo+t_Pt,t_Pt,2
blc4,-Ls/2-Lm+ok-0.9,jyo+t_Pt+2,1.8,Lb+(W_b/2-t_Pt/2)-2

numcmp,area
blc4,-Ls/2-Lm,jyo-(W_b/2-t_Pt/2),-Lb,W_b
blc4,-Ls/2-Lm,0,Lm,Wm/2
blc4,-Ls/2-Lm+ok-(W_b/2-t_Pt/2)-t_Pt/2,Wm/2,W_b,Lb
blc4,-Ls/2,,-t_Pt-ok,W_PLT/2
blc4,-Ls/2-ok,W_PLT/2,-t_Pt,Wm/2-W_PLT/2
blc4,-Ls/2-ok-t_Pt/2+0.9,Wm/2,-1.8,Lb
blc4,-Ls/2,Wm/2,-W_b,Lb

aadd,21,22,23! Pt near nanowire
aadd,18,20,19,24 ! All SiN platform   ! AREa 21 is SiN
asel,s,,,2,14
asel,a,,,16
aadd,all        ! Coil area is 18
allsel,all
numcmp,area
asba,5,4,,delete,keep
asba,7,6,,delete,keep  ! Splits into 8 and indu 5
asba,8,2,,delete,keep
asba,9,3,,delete,keep

k,1001,-20,Wm/2
```

```
k,1002,20,Wm/2
l,1001,1002

ASBL,      6,      31
APLOT

numcmp,area
! MESHING PHASE
mshape,1,2d  ! TRIANGULAR
esize,0.08
mat,3
amesh,1    ! Nanowire mesh

! Area 2,3,4,6 are material 4 or material 2

esize,0.4
mat,2
amesh,4  ! Coil

esize,1
amesh,2,3  !Pt on beams
esize,0.6
amesh,10    ! Pt near nanowire
esize,1
amesh,8


mat,1
esize,0.5
amesh,9
esize,0.8
amesh,5
esize,0.8
amesh,6
esize,1
amesh,7


! Generate Symmetric about Y axis
allsel,all
ARSYM,X,ALL, , , ,0,0
nsel,s,loc,x,-Ls/2-Lm-Lb-0.01,-Ls/2-Lm-Lb+0.01  ! LEFT END
d,all,TEMP,Tamb
nsel,s,loc,x,Ls/2+Lm+Lb-0.01,Ls/2+Lm+Lb+0.01  ! RIGHT END
d,all,TEMP,Tamb
nsel,s,loc,y,Wm/2+Lb-0.01,Wm/2+Lb+0.01
```

```
d,all,TEMP,Tamb
allsel,all
/sol
nsel,s,loc,y,0
SF,ALL,HFLUX,0
nsel,s,loc,y,Wm/2
nsel,r,loc,x,-Ls/2-Lm-Lb,-Ls/2-Lm,
SF,ALL,HFLUX,0
allsel,all

!RADIATION CONDN
SFL,78,HFLUX
SFL,80,HFLUX
SFL,87,HFLUX
SFL,96,HFLUX
SFL,142,HFLUX
SFL,165,HFLUX
SFL,69,HFLUX
SFL,85,HFLUX
SFL,155,HFLUX
SFL,167,HFLUX
SFL,83,HFLUX
SFL,88,HFLUX
SFL,151,HFLUX
SFL,166,HFLUX
! NANAOWIRE TOP BOUNDARY
SFL,3,HFLUX
SFL,35,HFLUX
SFL,150,HFLUX
SFL,156,HFLUX

eplot

! HEAT GENERATION
CURRENT=15e-6
Re1=2*(3.6e-10*(Tamb+20)+1.2e-7)*Lb/(1.8*tPt*1e-6)
Re2=2*(3.6e-10*(Tamb+10)+1.2e-7)*Lb/(t_Pt*tPt*1e-6)
BFA,12,HGEN,CURRENT*CURRENT*Re1/(tSiO+tSiN+tPt)/(1.8*Lb)     !Line heating
BFA,14,HGEN,CURRENT*CURRENT*Re2/(tSiO+tSiN+tPt)/(t_Pt*Lcoil)  !Coil Heating
ALLSEL,ALL
/prep7
nummrg,all
numcmp,node
/sol
solve
/post1
```

```
node1=8633
node2=11194
*GET,temp8633,NODE,8633,TEMP,
*GET,temp111,NODE,11194,TEMP,
tempdef=temp8633-temp111
PLNSOL, TEMP,, 0

! HEATING MEMBRANE DIAGRAM
allsel,all
nsel,s,loc,x,Ls/2,Lm
nsel,r,loc,y,0,Wm/2
ESLN,S
PLNSOL, TEMP,, 0
/EXPAND,2,RECT,HALF,,0.00001
/REPLOT

! SENSING MEMBRANE DIAGRAM
allsel,all
nsel,s,loc,x,-Lm,-Ls/2
nsel,r,loc,y,0,Wm/2
ESLN,S
PLNSOL, TEMP,, 0
/EXPAND,2,RECT,HALF,,0.00001
/REPLOT
```